2026 IEEE International Conference on Robotics and Automation (ICRA 2026)
June 1-5, 2026. Vienna, Austria

# Planning of Robotic High Intensity Focused Ultrasound Ablation via Predictive Models of Thermal Lesions*

F. Parrotta, *Student Member, IEEE*, I. Papagiannaki, S. Tognarelli, A. Diodato, and A. Menciassi, *Fellow, IEEE*

***Abstract* — High-Intensity Focused Ultrasound (HIFU) is a non-invasive therapeutic technology enabling precise energy delivery for the selective ablation of tumors, while preserving surrounding healthy tissue. Currently, there is no gold standard for defying sonication parameters to cover a tumor surface and volume, as this decision relies solely on the physician's experience. This work proposes a novel planning algorithm for robotic HIFU procedures that ensure automatic and optimized tumor coverage. The approach relies on a predictive model that estimates the dimensions of HIFU-induced thermal lesions based on sonication parameters (source pressure amplitude and sonication time) and leverages genetic algorithms to compute single lesion placement over the treatment area. The optimization function primarily aims to maximize the surface coverage over a defined target area and then integrates motion planning algorithms. In addition to planar lesions, a volumetric ablation composed by a set of co-planar surface lesions was also evaluated. The method was experimentally validated on ex-vivo tissues through a robotic ultrasound-guided (USg) HIFU platform. This study bridges pre-operative lesion prediction and intra-operative robotic execution, supporting standardized and effective HIFU therapy.**

## I. Introduction

High-Intensity Focused Ultrasound (HIFU) is an advanced, non-invasive therapeutic technology used for the treatment of various pathological conditions, such as malignant tumors and uterine fibroids [1], [2]. It operates by concentrating ultrasound waves to achieve millimeter-scale precision in targeting diseased tissues located deep within the body. The focused energy induces localized tissue necrosis through thermal and/or mechanical mechanisms, while preserving surrounding healthy structures [3]. By avoiding incisions and ionizing radiation, HIFU provides a safer and less invasive alternative to conventional treatment methods [4]. Recent advances in medical robotics have demonstrated that integrating the therapeutic transducer into a robotic platform enables precise and automated control of the HIFU beam, ultimately enhancing the accuracy and consistency of treatment delivery [5], [6].

Despite the technological improvements introduced by the integration of robotics, the selection of sonication parameters in HIFU treatments still relies on the physician's experience only. To move toward a more standardized and reproducible therapeutic protocol, predictive modeling can be employed [7], [8] to complement robotic precision with decision-making rigor. In particular, real-time models capable of predicting lesion formation can serve as a basis for automated treatment planning, enabling dynamic adaptation of HIFU delivery based on intraoperative conditions.

*This work was funded by "SURF-UP-Surgery by Using a Robotic Focused Ultrasound Platform" project under grant agreement no. FISA-2022-00770, within the Italina FISA programme—Fondo Italiano Scienze Applicate—HEALTH sector.

Effective implementation of these planning strategies requires robust optimization techniques to determine the optimal distribution of the single sonications across the treatment area [9], considering that in thermal HIFU treatment the resulting lesions exhibit an elliptical shape, characterized by a major axis $d_1$ and a minor axis $d_2$ [5].

In this context, Genetic Algorithms (GAs) provide a suitable framework for solving complex coverage problems in HIFU therapy [10]. GAs are population-based search and optimization techniques inspired by the principles of natural selection and heredity. By mimicking biological evolution, GAs operate through iterative cycles of selection to evolve increasingly optimal solutions [11]. Starting from a randomly generated population of candidate solutions, the algorithm evaluates everyone based on a fitness function - surface coverage of tumoral areas in this case - and uses genetic operators to create new generations. This process drives the population toward high-performing solutions that effectively balance multiple and potentially conflicting objectives. GAs are particularly well-suited for solving complex optimization problems that are nonlinear, high-dimensional, and lack analytical gradients [12]. Their versatility and robustness have made GAs widely applicable across fields such as robotics, machine learning, and decision-making [13]. In this work, we leverage GAs to compute optimal placements of elliptical lesions over a tumor surface, enabling automatic treatment coverage with high accuracy and adaptability.

To ensure successful lesion treatment, it is essential not only to achieve accurate coverage of the cancer lesion, but also to account for physiological factors such as tissue motion and blood perfusion. These phenomena can compromise treatment effectiveness, potentially leading to incomplete ablation. In this context, thermal HIFU planning requires the inclusion of lesion overlapping and a safety margin beyond the strict anatomical boundaries of the tumor. Overlapping sonications are used to reduce the risk of under-treatment, which may otherwise leave viable tumor tissue. High perfusion of tissues, for example, has been shown to reduce heating efficiency and create undertreated regions [9], while organ motion introduces spatial uncertainty in targeting. To mitigate these effects, increased overlap [14] and extended margins are often adopted, particularly in moving organs such as the liver or kidneys. The safety margin is specifically aimed at treating the tumor periphery and is carefully defined based on the proximity of surrounding anatomical structures. According to clinical practice, margins up to 10 mm beyond the tumor edge are commonly considered safe in clinical practice; however, a careful assessment of proximity to critical anatomical structures - e.g. blood vessels - remains essential [15], [16], [17].

Building on the technological potential offered by robotics, predictive modeling, and genetic-algorithm optimization, and considering the current limitations of HIFU planning, this study integrates thermal lesion prediction and intra-operative

robotic execution, supporting standardized and effective thermal HIFU therapy. By combining the benefits of robotic integration in non-invasive surgical procedures with numerical models for treatment prediction, the proposed approach aims to enhance both the accuracy and reproducibility of therapeutic outcomes.

The structure of this article is as follows: Section II describes the surface coverage optimization function, the experimental activities for algorithm validation, and the image analysis methods used to assess system outcome. Section III presents the results in terms of algorithm performance and experimental testing. Conclusions and future perspectives are provided in Section IV.

## II. Materials and Methods

The aim of this work is to demonstrate the accuracy of an optimization model, solved through a GAs–based approach, for the coverage of a tumoral region using HIFU technology. This section is structured as follows: (A) Description of the algorithm designed to optimize surface coverage within a predefined treatment area; (B) Description of the experimental setup employed to validate the proposed methods; and (C) quantitative lesion evaluation methods through image analysis techniques.

### *A. Surface coverage algorithm*

The aim of the algorithm is to maximize surface coverage by considering ellipses of variable size, while respecting boundary conditions on overflow and lesion overlap. The treatment domain is a circular disk considering three different diameters: (i) 15 mm; (ii) 20 mm; and (ii) 30 mm. These three conditions were selected based on clinical considerations: thermal ablation with HIFU is typically used to treat lesions with a volume not exceeding 3 cm³ [18]. Assuming a spherical shape, this corresponds to a lesion of approximately 18 mm in diameter.

The algorithm seeks to cover these regions using a set of elliptical ablations, each corresponding to a single HIFU delivery. Each sonication results in an elliptical lesion whose dimensions depend nonlinearly on the applied pressure and sonication duration. The major and minor axes of the ellipse - $d_1$ and $d_2$ - are calculated using a second-order polynomial model based on sonication time and source pressure amplitude [25], thus allowing the lesion size to vary dynamically during optimization according to the area to be covered. The ellipses are vertical, with fixed orientation, as the transducer is positioned parallel to their major axis. Each ellipse is parameterized by four variables:

- $C_x, C_z$: center coordinates of the ellipse (refer to Figure 1b)
- A *Scale Factor* that modulates the acoustic pressure (as a fraction of the maximum pressure achievable by the waveform generator used in the experimental setup)
- $t$: sonication time.

The number of ellipses, $N$, is varied within a specific interval to explore different trade-offs between treatment granularity and cumulative coverage. For each configuration, the variable vector $x \in \mathbb{R}^4$ represents all ellipse parameters.

The optimization algorithm is formulated to maximize the proportion of the target region that is covered by at least one ellipse; the coverage percentage is defined as the region covered by the ellipses compared to the target area. In addition to maximizing coverage, the algorithm accounts for two constraint functions:

- *Overflow*: the percentage of ablation that extends beyond a safety margin around the target boundary. The safety margin is defined as 10% of the diameter of the lesion under investigation. Although a 10 mm margin is typically adopted in clinical practice (as reported in the Introduction), in the proposed algorithm a smaller margin was employed in order to achieve higher target accuracy and avoiding injuries to the proximal healthy tissues.
- *Overlap*: the percentage of the target area that is ablated more than once. As blood perfusion can reduce heating effectiveness and lead to under-treated regions, controlled overlap is necessary to ensure complete ablation, while guaranteeing high coverage [19].

The constraints are defined as follows:

- $Coverage\ (x) \geq 90\%$
- $Overflow\ (x) < 3\%$
- $10\% \leq Overlap\ (x) \leq 30\%$ [14].

GAs are used to solve the constrained nonlinear optimization problem for each value of $N$. Boundaries are defined for each variable: the center coordinates $C_x$ and $C_z$ of each ellipse are constrained to lie within the circular treatment region of radius $R$. The Scale Factor is bound between 0.35 (106.6 kPa) and 0.65 (197.9 kPa), to ensure thermal treatment. These parameters are related to the experimental hardware, later described in Section II.B. The sonication time $t$, representing the duration of energy delivery, is allowed to vary between 0 and 10 seconds. For each target size, after evaluating all values in the specified range of $N$, the algorithm compares the obtained solutions and selects the configuration with the lowest cost. Therefore, the algorithm was run five times for each evaluated condition, to ensure that the final plan achieves the required coverage while using the smallest number of ellipses.

Specifically, the optimal solution is obtained through a genetic algorithm, implemented with the MATLAB function *ga()* provided by the Global Optimization Toolbox (MathWorks, Inc., USA). The function was called as `optVar=ga(objective,Number_of_variable*, [], [], [], [], lb, ub, nonlincon_handle, options)`, where the arguments were specified as follows. The objective function minimized the negative coverage percentage, thereby maximizing the lesion coverage. The number of variables was set to 4N, corresponding to the ellipse parameters: center coordinates, scale factor, and sonication time. Linear inequality and equality constraints were not required and thus left empty. The lower and upper bounds (lb, ub) constrained the ellipse centers, the scale, and the sonication time. The nonlinear constraint function evaluated each candidate solution to ensure that the covered area met the requirements, while respecting the limits on overflow and overlap. Finally, the options were set to a population size of 50, a crossover fraction of 0.8, elitism with 2 individuals per generation, a maximum of 2000 generations, and constraint tolerances of $10^{-8}$ and $10^{-6}$, respectively.

The final solution includes a set of optimized ellipses, which are sorted by vertical position $C_z$ to enable sequential robotic

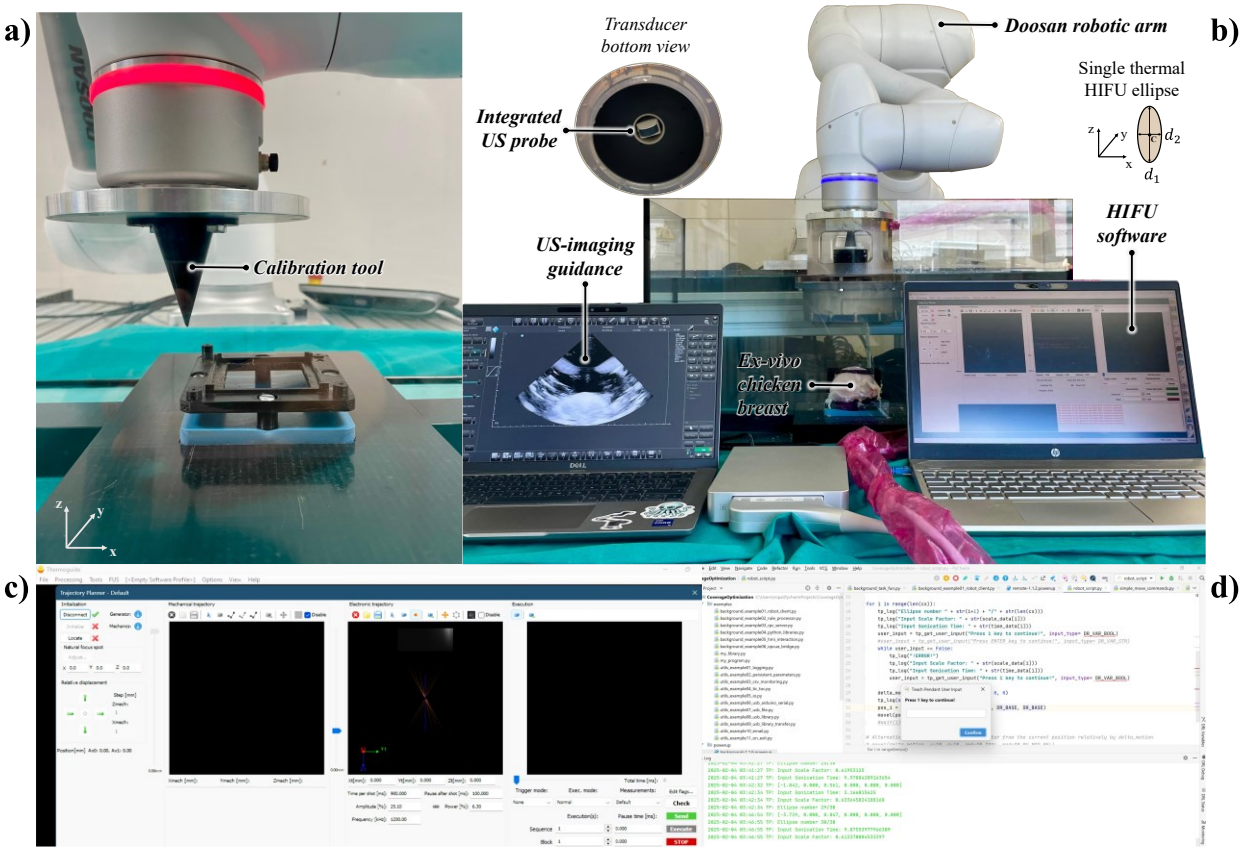


**Figure 1**. Experimental setup within the USgHIFU platform: (a) Calibration phase; (b) Robotic platform with the ex-vivo phantom aligned at the transducer focal length, i.e., with the phantom center placed at z =120 mm from the transducer; (c) HIFU software interface; (d) Robot motion control interface for automatic coverage of the target area.

HIFU treatment from the lower to the upper boundary of the target. This strategy prevents excessive overtreatment [20] , and at the same time minimizes acoustic aberrations [21], as tissue properties change because of lesion formation.

The output of the described algorithm is a structured list of parameters - ellipse center coordinates, scale factors, and sonication times - where the spatial coordinates serve as input for robotic positioning, while the sonication parameters are provided to the waveform generator control software to modulate acoustic energy delivery.

### *B. Experimental validation*

HIFU experiments were conducted with a robotic USgHIFU platform shown in Figure 1. The system incorporates a 6-degree-of-freedom robotic arm (M0609, Doosan, Korea) holding the therapeutic HIFU transducer - an annular 16-channel phased array with a central frequency of 1.2 MHz, an external diameter of 120 mm, and a focal length of 120 mm (Imasonic, Voray-sur-l'Ognon, France). The transducer is powered by a 16-channel high-power signal generator (Image Guided Therapy, Pessac, France), capable of delivering up to 20 W per channel, for a total maximum output of 320 W - corresponding to a maximum acoustic pressure of 304.6 kPa, according to the quadratic relationship that links power [W] to source pressure amplitude [Pa] [22]. For treatment monitoring, the HIFU transducer is integrated with a confocal 2D phased-array ultrasound probe (P5-1S15A-6, Telemed, Vilnius, Lithuania), which provides real-time visual feedback during targeting and therapy. De-ionized and degassed water (dd-$H_2O$) was used as the coupling medium to ensure proper ultrasound beam propagation from the transducer to the ex-vivo phantom. A dedicated water tank was employed as the treatment workspace, and an ex-vivo chicken breast phantom was positioned at its base. This setup ensured complete immersion of the phantom in water, and included an integrated acoustic absorber placed beneath the tissue to minimize wave reflections [23].

Robot motion for the USgHIFU ablation task was programmed in Python 3.5 using DRL Studio. The control input of the USgHIFU system was defined by the surface coverage optimization algorithm. Specifically, it included (i) the target sonication points for the robotic manipulator, given as 2D coordinates of the ellipses' centers (representing the predicted thermal lesion locations), and (ii) the parameters for the HIFU signal generator, namely sonication duration and an energy scaling factor. Prior to execution, a spatial calibration procedure (Figure 1a) was carried out to compute the rigid transformation between the robot base frame and the sample coordinate frame (i.e. black frame in Figure 1a). The method is based on matched point registration between robot-measured coordinates and known groove positions on a 3D-printed calibration frame [24]. Following calibration, the geometric focus of the HIFU transducer was aligned with the center of the tissue sample. This reference point was defined as the origin (0, 0) of the sonication disk. All planned sonication coordinates were expressed relative to this origin,

allowing the robot to execute each movement as an offset from the calibrated center. During execution, the robot followed a bottom-up sonication sequence to reduce acoustic aberration caused by preheated tissue, as introduced in Section II.A.

At each step, the system moved the transducer to the designated target pose and published the corresponding sonication parameters. Execution paused until a binary input was provided by the user. Entering '1' allowed the system to proceed to the next pose; any other input triggered an error message and prompted a retry. The procedure could be interrupted at any time by terminating the program. A fixed pause of 15 seconds was inserted after each sonication before continuing to the next ellipse.

3 experimental conditions were tested, corresponding to treatment areas with diameters of 15mm, 20 mm, and 30 mm, respectively. Lesions were realized in the x-z plane, considering the transducer focal length of 120 mm between the transducer and the phantom center, thus producing a lesion at tissue depth. For each case, the ablation was repeated three times.

Furthermore, starting from the geometric assumption that a cylindrical volume can be decomposed into a sum of successive disks, a volumetric lesion with cylindrical geometry was evaluated by repeating the 15 mm circular ablation to form a 15 mm-high cylinder along the y-axis, considering a mean thickness of 3 mm for each disk. Based on this assumption, the study also explored the possibility of translating the optimized 2D algorithm into a volumetric ablation strategy. The volumetric test also investigated the possibility of leaving an untreated region between two ablation volumes. Specifically, the first cylinder was created by generating five consecutive disks in the x-z plane, considering a 3 mm (thickness of each disk) axial shift along the y-axis between the centers of successive disks. A gap was then introduced through robotic displacement, after which a second identical cylinder was produced. This experiment was repeated three times as well.

All the resulting lesions were analyzed using a digital microscope (HRX-01 3D, Hirox-USA), equipped with an MX-MACROZ IV lens (20× magnification).

### *C. Quantitative lesion evaluation*

This section describes how the lesions obtained from the experimental activity were quantitatively evaluated and used for comparison with the results produced by the proposed algorithm. To this end, the percentage of ablated tissue was quantified on the images acquired with the microscope, specifically by measuring the white-colored region relative to the surrounding untreated tissue. The images obtained from the microscope include a 5 mm scale bar, which was used in a MATLAB script to calculate the spatial resolution in millimeters per pixel.

The image is then converted to grayscale, and a brightness-based thresholding approach is used to detect the ablated tissue. The grayscale image was first normalized to the [0,1] range to standardize pixel intensity values. A brightness threshold corresponding to the 85th percentile was then applied to isolate the top 15% brightest pixels, that should represent thermally affected tissue. A binary mask was generated to segment these high-intensity regions. To ensure the inclusion of diffusely ablated tissue, the mask is expanded using morphological dilation. Within this mask, an intensity-weighted centroid was computed to estimate the center of mass of the ablation zone, under the assumption that thermal damage results in increased local brightness. This step prevents the exclusion of tissue regions that were effectively treated but appear with lower intensity in the image. Finally, a circular region of interest (ROI) is drawn centered at the computed center of mass with a radius matching the expected lesion size. The proportion of pixels identified as ablated within the ROI is then computed as a percentage of the theoretical lesion area. This value represents the experimentally observed coverage and is used as a ground-truth metric for comparison with the predicted coverage produced by the optimization algorithm. As a final step, a concentric circular region is drawn with a diameter increased by 10% compared to the original, corresponding to the safety margin also considered in the optimization algorithm.

## III. Results

The following paragraphs present the achieved results in terms of (A) Performances of the surface coverage algorithm; (B) Planar ablation tests whose outcomes were evaluated through image analysis, with the aim of quantifying the experimental outcome and comparing it with the predicted lesion; and (C) Volumetric ablation test.

### *A. Surface coverage planning performances*

The optimization algorithm covers the target area using a set of ellipses, identifying the minimum number N required to achieve maximum surface coverage. Specifically, a coverage of (i) 97.15% with N=25 was obtained for the 15 mm diameter circle; (ii) 96.62% with N=23 for the 20 mm diameter circle; and (iii) 99.56% with N=24 for the 30 mm diameter circle. Overlap is greater than 28% in all solutions. An example of the resulting coverage produced by the algorithm is shown in Figure 2.

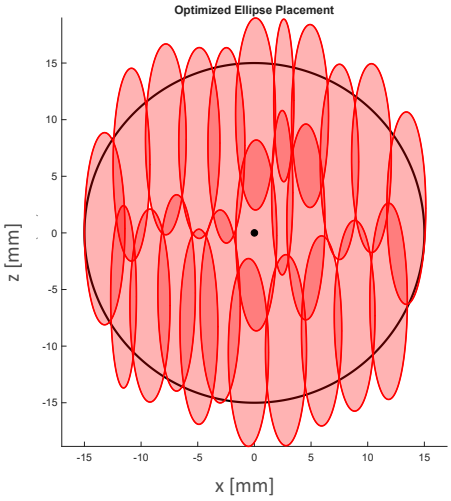


**Figure 2**. Example of surface coverage output from the MATLAB implementation of the genetic algorithm-based method in a 30 mm lesion, assuming a mean disk thickness of 3 mm.

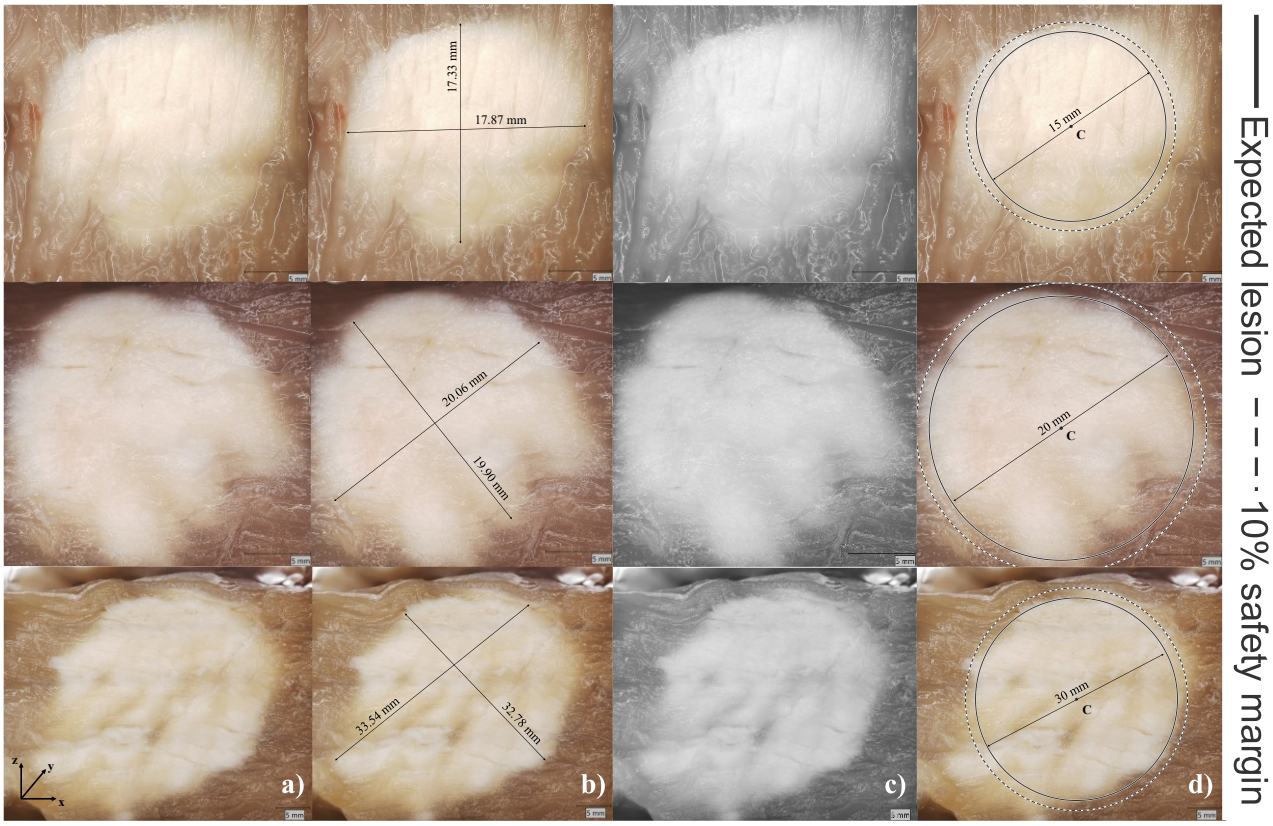


**Figure 3.** Experimental results: (a) Images acquired with the digital microscope (HRX-01 3D; Hirox-USA); (b) Digital microscope images, with measurements based on the outermost ablation points; (c) Grayscale image for brightness-based evaluation of the ablated area; and (d) Target area evaluation considering the safety margin (dashed line). The center of the circular lesion (C) is located at the center of the ex-vivo chicken breast phantom. The distance between point C and the transducer corresponds to its focal length of z = 120 mm.

### *B. Planar ablation tests*

Ablation tests were assessed through digital microscope imaging (HRX-01 3D; Hirox-USA), with the outcomes shown in Figure 3**.** Starting with the 15 mm target, the measured coverage from images (described in Section II.D) was 98.09%, while the simulation predicted 97.15%, with a difference of 0.93%. For the 20 mm target, image analysis revealed a coverage of 95.52%, with the ablation fully contained within the predefined safety margins. The corresponding MATLAB simulation predicted a coverage of 96.62%, showing a deviation of 1.1%. For the 30 mm target, the measured coverage was 98.55%, while the simulation predicted 99.56%, with a difference of 1.01%. For areas of 15 mm and 30 mm, the ablation pattern slightly exceeded the safety margins, as illustrated in Figure 4. However, the overflow remained within the acceptable clinical limits, i.e., up to 10 mm beyond the tumor boundary. The deviations between predicted and observed lesion shapes are mainly attributed to tissue movement during the experimental setup, which can lead to targeting inaccuracies. In fact, as shown in Figure 4, this effect is recognizable from some of the elliptical shapes appearing shifted with respect to the circular target. Additional limitations encountered during testing included challenges in precise tissue cutting, since the thermal lesions are in the tissue depth and therefore externally invisible. Despite these factors, the experimental results closely matched the coverage performance predicted by the optimization algorithm.

### *C. Volumetric ablation tests*

As introduced in Section II.B, the volumetric ablation tests consisted of two cylindrical lesions with an expected base diameter of 15 mm and an axial height of 15 mm, separated by a 15 mm untreated region. Considering thickness of 3 mm for each disk, each cylinder was therefore realized as a stack of five consecutive disks.

After three repetitions under the same experimental conditions, the resulting lesions exhibited an effective axial length of approximately 23 mm and an untreated gap of about 10 mm, thus presenting a variation of about 50%. These dimensions were assessed on the axial plane of the cylinder, as shown in Figure *5*.

The lesion axial elongation observed in the volumetric tests (plane A–A in Figure 5) was investigated by modeling the thermal diffusion length between successive planes. According to the Pennes' bioheat equation [26], heat transfer in tissue results from conductive diffusion and a perfusion-related sink term. In ex-vivo conditions, the perfusion contribution is absent, and heat transport is governed by conduction only.

Heat conduction can be described by a Gaussian profile, with the thermal diffusion length defined as $L_{diff} = \sqrt{4\alpha\tau}$ [27], where $\alpha\ [mm^2/s]$ represents the thermal diffusivity coefficient of the tissue and $\tau\ [s]$ accounts for sonication time. Therefore, $L_{diff}$ represents the characteristic diffusion length, i.e., the radial distance over which heat propagates from the

focal spot within the characteristic time $\tau$. If focal centers are spaced closer than $2L_{diff}$, temperature fields overlap, and thermal accumulation occurs [28].

In the specific case of the volumetric ablation tests, each disk produces thermal diffusion along the axial direction of the cylinder, extending from its center by $L_{diff}$. In the internal regions, overlapping exposures increase the thermal dose, thus leading to overtreatment. Thermal damage therefore accumulates in a nonlinear manner, while decaying exponentially with distance. In contrast, the two external disks (first and fifth) determine the effective extension of the nominal boundaries. Considering an effective sonication time for each disk of $\tau = 48\ s$ (excluding cooling intervals) based on the presented coverage algorithm, and $\alpha = 0.14\ mm^2/s$ for ex-vivo tissues [29], $L_{diff} \cong 5.2\ mm$ on each side. Since this distance is measured from the focal spot, half of the disk's thickness should be subtracted from $L_{diff}$ when calculating the effective overshoot. This results in:

$$L_{overshootAxial} = L_{diff} - 1.5 = 3.7\ mm$$

This results in a total axial length of the lesion equal to:

$$L_{axial} = 15\ mm + 2L_{overshootAxial} \cong 22.4\ mm.$$

This analysis agrees with the experimental measurements (Figure 5) indicating that the observed axial enlargement - beyond experimental variability - can be primarily attributed to thermal stacking, as formalized by this model. Moreover - as also mentioned in the Introduction - tissue aberrations should be taken into account. Since each sonication modifies the local thermal and acoustic properties, closely spaced exposures may partially act on progressively altered tissue. Unlike thermal stacking, aberrations represent a phenomenon that is difficult to quantify [30].

What has been described so far in this paragraph refers to the axial plane of the cylinder (plane A–A in **Figure 5**), but the same rationale applies also to the radial one (plane B–B in Figure 5). In this case, the increase with respect to the predicted dimensions is about 20%. To estimate the radial overshoot, only the two outermost ellipses were considered, with sonication times of 2.5 s (Scale Factor = 0.65) and 1.7 s (Scale Factor = 0.65), yielding to diffusion lengths of $L_{diff1} = 1.18\ mm$ and $L_{diff} = 0.97\ mm$, respectively. From the predictive polynomial model, the corresponding values for the minor dimension of the ellipses $d_2$ were 1.45 mm and 1.10 mm. This results in:

$$L_{overshootRadial} = L_{overshootRadial1} + L_{overshootRadial2}$$
$$L_{overshootRadial1} = L_{diff1} - {}^{1.45}/_{2} = 0.46\ mm$$
$$L_{overshootRadial2} = L_{diff2} - {}^{1.10}/_{2} = 0.42\ mm$$

Accordingly, the resulting radial diffusion length is:

$$L_{radial} = 15\ mm + L_{overshootRadial} \cong 15.9\ mm.$$

When referring back to the results reported in Section II.B, the radial enlargement on the considered plane was present, but not deepened as the geometrical extension remained within the clinical safety margins.

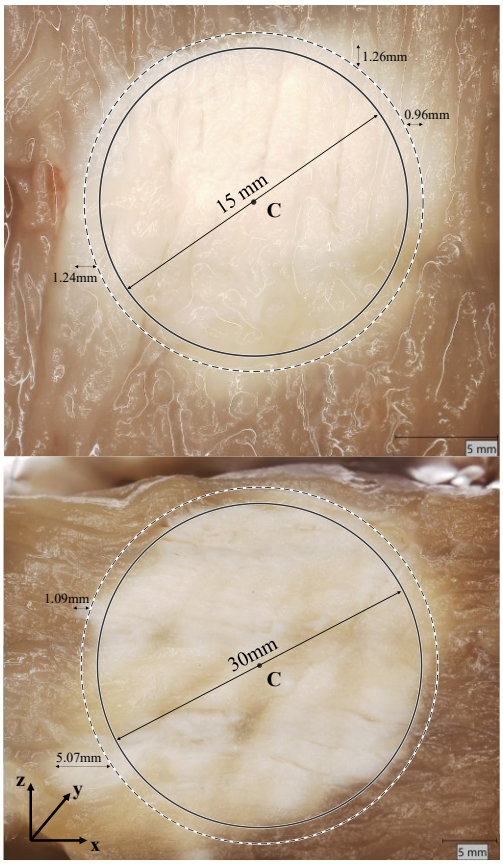


**Figure 4.** Overflow assessment for: (a) 15 mm target area; and (b) 30 mm target area. Due to tissue movement during the experimental tests, the ablation exceeded the safety margin considered in the algorithm, while remaining within the clinically accepted safe guidelines [15], [16], [17]. The center of the circular lesion (C) is located at the center of the ex-vivo chicken breast phantom. The distance between point C and the transducer corresponds to its focal length of z = 120 mm (as in Figure 3).

## IV. Discussion and Conclusion

The definition of HIFU sonication parameters for tumor coverage relies on the physician's experience, with no established standard for thermal treatment planning. Previous works in literature explored predictive models [7], [8] or robotic integration [5], [6] separately. In this work, we demonstrated the feasibility of a genetic algorithm-based planning approach that integrates experimentally validated lesion prediction models with robotic USgHIFU execution, achieving highly accurate target coverage.

The proposed method showed coverage rates of 97.15%, 96.62% and 99.56% for 15 mm, 20 mm and 30 mm treatment areas respectively, while maintaining overflow and overlap within clinically acceptable margins [14], [19]. Experimental validation on ex-vivo tissues confirmed close agreement between predicted and actual ablation outcomes, with errors between the algorithm and the experimental measurements of 0.93%, 1.10% and 1.01% for the three mentioned conditions. Slight deviations were mainly attributed to tissue movement,

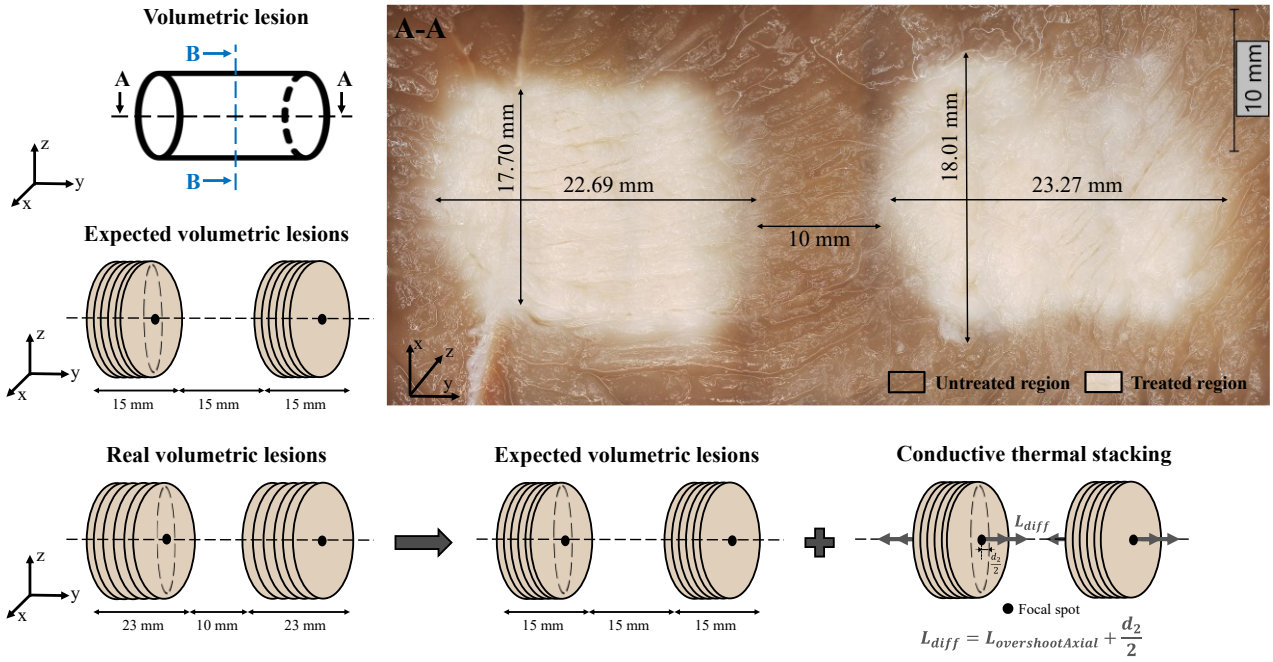


**Figure 5.** Volumetric lesion evaluation: plane A–A represents the axial development of the lesion, whereas plane B–B illustrates the radial development of the volumetric ablation. The obtained volumetric lesion showed an enlargement compared to the predicted size. The figure illustrates the distance of heat propagation from the focal spot, resulting from cumulative conduction phenomena within the tissue due to the absence of blood perfusion in ex-vivo phantoms.

which led to targeting inaccuracies during execution – a common challenge in ex-vivo HIFU procedures. Another critical factor during experimental validation is the ability to cut the tissue along the correct plane to fully visualize the lesion, since the treatment is completely invisible from the outside. This needs to be considered when evaluating the differences between the expected and the effective lesion dimensions.

The integration of real-time predictive lesion models into the optimization process enables dynamic adaptation of sonication parameters (i.e. source pressure amplitude and sonication time), allowing the algorithm to tailor ablation patterns to the target's geometry. Moreover, a sequential bottom-up sonication strategy is adopted to minimize acoustic aberrations from preheated tissue [21], [30].

In addition to planar lesions, the possibility of generating a volumetric ablation as the sum of successive planar ablations was also investigated, even considering that the algorithm was optimized for surface coverage. The resulting volumetric dimensions exceeded the expected values by approximately 50% on the axial plane and 20% on the radial one. This phenomenon was studied by referring to Pennes' bioheat equation [26]. In this framework, the heat accumulated by conduction in the tissue would normally be dissipated through blood perfusion. However, the experimental tests were performed on ex-vivo tissues, where the perfusion term is absent. For this reason, a mathematical analysis based on thermal diffusion was conducted, showing that conductive mechanisms led to an overall increase of the planned size. The same analysis was applied to the previously discussed planar results. Also in these cases an enlargement in lesion size would also be expected, although less pronounced due to the lower total number of sonications. Nevertheless, the extension remains within the safe thresholds defined by the clinical safety margin. Although the polynomial model underlying the 2D optimization incorporated thermal effects through multiphysics simulation and was experimentally validated on single lesions, these findings indicate that its translation to 3D leads to discrepancies due to cumulative conductive phenomena. This limitation is particularly evident in ex-vivo tissues, where the absence of blood perfusion prevents heat removal and makes conductive mechanisms the dominant factor in lesion growth.

The results presented in this study highlight the critical role of thermal accumulation in determining lesion dimensions. Future work will mainly address this aspect. In particular, the observed axial elongation could be explained by conductive thermal diffusion, and for this reason next developments will explicitly incorporate the accumulation of heat through conduction in the optimization function, thereby improving predictive accuracy. In addition, to further investigate the underlying thermal mechanisms, experimental validation will be extended to perfused tissue, to fully replicate physiological conditions and provide accurate treatment prediction.

To conclude, this work represents a step forward standardized and automated robotic USgHIFU therapy, demonstrating that predictive modeling combined with optimization-based planning can achieve high coverage performance while respecting clinical safety constraints. By providing a systematic and repeatable framework for coverage planning, the proposed approach reduces reliance on operator expertise and supports procedural standardization. This paradigm provides the basis for future clinical translation, bridging the gap between preoperative planning and autonomous intraoperative execution.

## REFERENCES


[1] "Home - Focused Ultrasound Foundation." Accessed: Jul. 31, 2025. [Online]. Available: https://www.fusfoundation.org/

[2] S. Mihcin and A. Melzer, "Principles of focused ultrasound," *Minim. Invasive Ther. Allied Technol.*, vol. 27, no. 1, pp. 41–50, Jan. 2018, doi: 10.1080/13645706.2017.1414063.

[3] G. Ter Haar, "Ultrasound focal beam surgery," *Ultrasound Med. Biol.*, vol. 21, no. 9, pp. 1089–1100, 1995, doi: 10.1016/0301-5629(95)02010-1.

[4] C. R. Hill, J. C. Bamber, and G. R. Ter Haar, "Physical Principles of Medical Ultrasonics," *Physical Principles of Medical Ultrasonics*, pp. 1–511, Oct. 2005, doi: 10.1002/0470093978.

[5] A. Mariani, L. Morchi, A. Diodato, S. Tognarelli, and A. Menciassi, "High-Intensity Focused Ultrasound Surgery Based on KUKA Robot: A Computer-Assisted Platform for Noninvasive Surgical Treatments on Static and Moving Organs," *IEEE Robot. Autom. Mag.*, vol. 30, no. 3, pp. 79–93, Sep. 2023, doi: 10.1109/MRA.2022.3188221.

[6] A. Gunderman, R. Montayre, A. Ranjan, and Y. Chen, "Review of Robot-Assisted HIFU Therapy," *Sensors 2023, Vol. 23, Page 3707*, vol. 23, no. 7, p. 3707, Apr. 2023, doi: 10.3390/S23073707.

[7] B. E. Treeby and B. T. Cox, "k-Wave: MATLAB toolbox for the simulation and reconstruction of photoacoustic wave fields," *J. Biomed. Opt.*, vol. 15, no. 2, p. 021314, 2010, doi: 10.1117/1.3360308,.

[8] P. Montienthong and P. Rattanadecho, "Focused ultrasound ablation for the treatment of patients with localized deformed breast cancer: Computer simulation," *J. Heat Transfer*, vol. 141, no. 10, Oct. 2020, doi: 10.1115/1.4044393.

[9] S. Lari, M. Kohandel, and H. J. Kwon, "Model based deep learning method for focused ultrasound pathway scanning," *Sci. Rep.*, vol. 14, no. 1, Dec. 2024, doi: 10.1038/s41598-024-70689-9.

[10] F. Tossa, W. Abdou, E. C. Ezin, and P. Gouton, "Improving Coverage Area in Sensor Deployment Using Genetic Algorithm," *Computational Science – ICCS 2020*, vol. 12141, p. 398, 2020, doi: 10.1007/978-3-030-50426-7_30.

[11] I. Costa-Carrapiço, R. Raslan, and J. N. González, "A systematic review of genetic algorithm-based multi-objective optimisation for building retrofitting strategies towards energy efficiency," *Energy Build.*, vol. 210, p. 109690, Mar. 2020, doi: 10.1016/J.ENBUILD.2019.109690.

[12] S. Katoch, S. S. Chauhan, and V. Kumar, "A review on genetic algorithm: past, present, and future," *Multimed. Tools Appl.*, vol. 80, no. 5, p. 8091, Feb. 2020, doi: 10.1007/S11042-020-10139-6.

[13] A. Lambora, K. Gupta, and K. Chopra, "Genetic Algorithm- A Literature Review," *Proceedings of the International Conference on Machine Learning, Big Data, Cloud and Parallel Computing: Trends, Prespectives and Prospects, COMITCon 2019*, pp. 380–384, Feb. 2019, doi: 10.1109/COMITCON.2019.8862255.

[14] J. Barkin, "High intensity focused ultrasound (HIFU)," 2011.

[15] M. Alabousi and S. Ghai, "Magnetic resonance imaging-guided ultrasound ablation for prostate cancer – A contemporary review of performance," Jan. 04, 2023, *Frontiers Media S.A.* doi: 10.3389/fonc.2022.1069518.

[16] E. J. Aslim *et al.*, "Defining prostate cancer size and treatment margin for focal therapy: does intralesional heterogeneity impact the performance of multiparametric MRI?," *BJU Int.*, vol. 128, no. 2, pp. 178–186, Aug. 2021, doi: 10.1111/BJU.15355.

[17] J. S. Wysock and H. Lepor, "Optimizing patient selection for focal therapy—mapping and ablating the index lesion," *Transl. Androl. Urol.*, vol. 7, no. Suppl 4, pp. S519–S525, Sep. 2018, doi: 10.21037/TAU.2018.03.16.

[18] Published by Focused Ultrasound Foundation, "Focused Ultrasound and Cancer Immunotherapy Workshop - White Paper Summary," Jul. 2023.

[19] E. Sassaroli, K. C. P. Li, and B. E. O'Neill, "Modeling Focused Ultrasound Exposure for the Optimal Control of Thermal Dose Distribution," *The Scientific World Journal*, vol. 2012, p. 252741, 2012, doi: 10.1100/2012/252741.

[20] F. A. Schmid *et al.*, "Prospective multicentre study using high intensity focused ultrasound (HIFU) for the focal treatment of prostate cancer: Safety outcomes and complications," *Urologic Oncology: Seminars and Original Investigations*, vol. 38, no. 4, pp. 225–230, Apr. 2020, doi: 10.1016/J.UROLONC.2019.09.001.

[21] G. P. L. Thomas, T. D. Khokhlova, O. A. Sapozhnikov, Y. N. Wang, S. I. Totten, and V. A. Khokhlova, "In Vivo Aberration Correction for Transcutaneous HIFU Therapy Using a Multielement Array," *IEEE Trans. Ultrason. Ferroelectr. Freq. Control*, vol. 69, no. 10, pp. 2955–2964, Oct. 2022, doi: 10.1109/TUFFC.2022.3200309.

[22] F. Wu, G. ter Haar, and I. Rivens, "Image-guided Focused Ultrasound Therapy," *Image-guided Focused Ultrasound Therapy*, Jun. 2024, doi: 10.1201/9780429162671/IMAGE-GUIDED-FOCUSED-ULTRASOUND-THERAPY-FENG-WU-GAIL-TER-HAAR-IAN-RIVENS.

[23] A. Diodato, A. Cafarelli, A. Schiappacasse, S. Tognarelli, G. Ciuti, and A. Menciassi, "Motion compensation with skin contact control for high intensity focused ultrasound surgery in moving organs," *Phys. Med. Biol.*, vol. 63, no. 3, p. 035017, Jan. 2018, doi: 10.1088/1361-6560/AA9C22.

[24] K. Van Wyk and J. A. Marvel, "Strategies for Improving and Evaluating Robot Registration Performance," *IEEE Trans. Autom. Sci. Eng.*, vol. 15, no. 1, p. 10.1109/TASE.2017.2720478, Jan. 2018, doi: 10.1109/TASE.2017.2720478.

[25] F. Parrotta, S. Tognarelli, and A. Menciassi, "A Polynomial Model for Estimation of Ex-Vivo HIFU Thermal Lesion Dynamics Based on Pressure Amplitude and Sonication Time," *Applied Sciences*, vol. 16, no. 4, p. 1847, Feb. 2026, doi: 10.3390/app16041847.

[26] H. H. Pennes, "Analysis of tissue and arterial blood temperatures in the resting human forearm," *J. Appl. Physiol.*, vol. 85, no. 1, pp. 5–34, 1998, doi: 10.1152/JAPPL.1998.85.1.5,.

[27] S. L. Angioni, F. Ciampa, F. Pinto, G. Scarselli, D. P. Almond, and M. Meo, "An Analytical Model for Defect Depth Estimation Using Pulsed Thermography," *Exp. Mech.*, vol. 56, no. 6, pp. 1111–1122, Jul. 2016, doi: 10.1007/S11340-016-0143-4/FIGURES/7.

[28] Y. Zhou, "Generation of uniform lesions in high intensity focused ultrasound ablation," *Ultrasonics*, vol. 53, no. 2, pp. 495–505, Feb. 2013, doi: 10.1016/J.ULTRAS.2012.09.001.

[29] S. R. Guntur, K. Il Lee, D. G. Paeng, A. J. Coleman, and M. J. Choi, "Temperature-Dependent Thermal Properties of ex Vivo Liver Undergoing Thermal Ablation," *Ultrasound Med. Biol.*, vol. 39, no. 10, pp. 1771–1784, Oct. 2013, doi: 10.1016/J.ULTRASMEDBIO.2013.04.014.

[30] P. B. Rosnitskiy, T. D. Khokhlova, G. R. Schade, O. A. Sapozhnikov, and V. A. Khokhlova, "Treatment Planning and Aberration Correction Algorithm for HIFU Ablation of Renal Tumors," *IEEE Trans. Ultrason. Ferroelectr. Freq. Control*, vol. 71, no. 3, pp. 341–353, Mar. 2024, doi: 10.1109/TUFFC.2024.3355390,.